

Stationary two-qubit entanglement mediated by one-dimensional plasmonic nanoarrays

Luke C. Ugwuoke,^{1,*} Tjaart P. J. Krüger,^{2,3} and Mark S. Tame¹

¹*Department of Physics, Stellenbosch University, Private Bag X1, Matieland 7602, South Africa.*

²*Department of Physics, University of Pretoria, Private Bag X20, Hatfield 0028, South Africa.*

³*National Institute for Theoretical and Computational Sciences (NITheCS), South Africa.*

(Dated: December 19, 2025)

Entanglement is one of the key measures of quantum correlations present in nanophotonic systems, with promising applications in quantum optics and beyond. Previous studies have shown that the degree of entanglement between two quantum dot qubits is preserved when a metal nanoparticle is used to mediate the interactions between the qubits. In this work, we investigate long-range plasmonic mediation of qubit–qubit entanglement by studying the impact of the number of mediating metal nanoparticles on stationary concurrence. Collinear and periodically spaced metal nanoparticles that satisfy the weak-coupling approximation are considered. An effective model that enables the derivation of the mediated interactions within the framework of cavity quantum electrodynamics is employed. Under weak driving at the single particle resonance frequency, the model shows that odd-number arrays are more robust to entanglement decay. We attribute this to strong inter-qubit dissipative coupling as a result of a hybridized dipole plasmon resonating with the driving frequency in odd-number arrays. These arrays can sustain non-vanishing stationary entanglement beyond an inter-qubit spacing of one micron, opening up the possibility of independent spatial optical probing of each quantum dot.

I. INTRODUCTION

In recent years, quantum correlation metrics, such as discord [1, 2], entanglement [3–6], steering [7, 8], and second-order coherence [9, 10], have become very useful for investigating non-classical phenomena in quantum systems. Among these metrics, entanglement—where two or more interacting quantum systems are in a shared state—is widely studied as a measure of quantumness in atomic systems [11], nanophotonic systems [10, 12–14], and beyond [15]. The huge interest in entanglement research can be attributed to the many potential applications of the strong quantum correlations possessed by entangled states. For example, entangled photon states have been used to enhance the sensing precision in biosensing [16–20] and image resolution in quantum imaging [21, 22], as well as to develop reliable cryptographic keys for secure quantum communication channels [23–25]. Entanglement has also been found to play a significant role in the performance of quantum machines [15, 26, 27], high-speed quantum computations [28, 29], and quantum teleportation networks [30, 31].

Quantum dots (QDs) are nanoscale semiconductor materials with size-dependent electromagnetic properties [32–35]. They have discrete electronic or spin states that can be accessed to create a qubit—a quantum system with two levels [33–35]. Two QD qubits may then be entangled either directly or indirectly by interacting with a mediator [36]. Several studies have investigated the interaction between a QD and a metal nanoparticle (MNP), where semiclassical effects such as exciton–plasmon coupling [9, 36, 37] and quantum effects such as interference-induced two-photon correlation [9, 38–40] and resonance fluorescence [9, 41] have been reported. Both classical and non-classical effects have also been studied in coupled systems consisting of a QD and a one-dimensional MNP array [42–44], where the ability of a MNP array to

support collective plasmon resonances, as well as confine and transport electromagnetic energy across the nanoparticle chain [45–55], is utilized in enhancing QD absorption [42], Purcell enhancement [43], and single-photon generation [44].

Plasmon-mediated bipartite entanglement involves the use of exciton–plasmon coupling between a plasmonic material—the mediator—and a pair of excitonic qubits to generate entangled states under certain conditions [12, 56–62]. Due to the inherent ohmic losses present in plasmonic systems, entanglement generation in QD qubits via plasmon-mediated interactions is limited to states that are not maximally-entangled [12, 58, 62]. Hence, mediated entanglement is actively being researched, with mediators ranging from single MNPs [12, 56–58] to waveguides [14, 61–63].

Pioneering work in quantum plasmonics showed that polarization-entangled states can be preserved via surface plasmons [64, 65], while recent studies have focused on entanglement generation via plasmonic mediation [6, 58, 62], as well as entanglement stabilization [14, 66]. With a single MNP, the underlying theory of MNP-mediated entanglement has been well established [12, 56]. On the other hand, mediators with waveguiding capabilities aim to sustain qubit–qubit entanglement over large inter-qubit distances where long-range plasmonic coupling due to a single MNP is no longer sufficient to prevent decoherence and the subsequent loss of entanglement [61–63]. Previous work has also proposed a scheme for long-range two-qubit entanglement generation using a two-arm MNP array, assisted by nanowire waveguides [13]. Though efficient, the scheme does not utilize plasmon-mediated inter-qubit interactions, and relies on post-selection, making it hard to realize [13].

In this work, we study the generation of stationary two-qubit entanglement solely via mediated qubit–qubit interactions due to the coupling of the qubits to collective plasmon resonances in a one-dimensional plasmonic nanoarray, and investigate the dependence of the concurrence [3, 67]—a direct entanglement measure for two-qubit systems—on the number, n , of MNPs in the array. Previous studies have used

* lcugwuoke@gmail.com

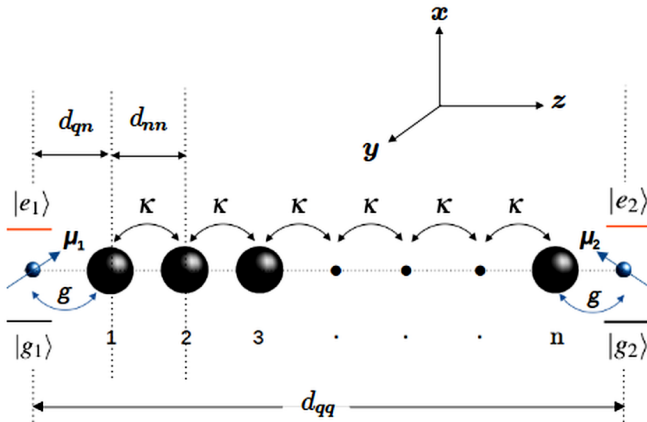


FIG 1. (Color online) Geometry of the QD-NA-QD system. A one-dimensional MNP array is sandwiched by two QD qubits, with dipole moments μ_1 and μ_2 , respectively. The center-to-center distance between each QD and the nearest MNP is d_{qn} . The MNPs in the array are spaced periodically with a center-to-center distance denoted as d_{nn} . As the number n of MNPs in the array increases, the qubit–qubit separation, d_{qq} , increases. Nearest-neighbor couplings are represented by the QD-MNP dipole–dipole coupling rate g and the MNP-MNP dipole–dipole coupling rate κ . Each QD qubit has ground and excited states denoted as $|g_i\rangle$ and $|e_i\rangle$ ($i = 1, 2$), respectively.

the Green's tensor approach to study mediated interactions due to groove-on-metal [10, 61, 62] and parallel nanowire [63] waveguides. Here, we employ a slightly less cumbersome, but equally reliable approach, based on the effective model previously used in Refs. [56, 59, 66], to obtain the mediated interactions due to a MNP array waveguide.

This paper is organized as follows. The geometry and other parameters of the model, including Hamiltonians, dissipators, and coupling rates of the MNP-MNP and QD-MNP dipole–dipole interactions, are discussed in Sec. II. In Sec. III, plasmon-induced terms and mediated coupling rates of the qubits are derived and explained within an effective picture formulation. The effective parameters of the qubits are transformed to the Dicke basis and discussed in Sec. IV, with emphasis on the parameters due to even- n and odd- n arrays. Also, in Sec. IV, the mediated stationary entanglement is discussed and the concurrences due to even and odd n -array mediators are compared. A comparison between numerical simulations and the effective model is also provided in Sec. IV, before the conclusion of the paper in Sec. V.

II. MODEL GEOMETRY AND PARAMETERS

The system we consider is shown in Fig. 1. It consists of two QD qubits sandwiching a metal nanoparticle array (NA) at an inter-qubit center-to-center distance denoted by d_{qq} . The NA consists of periodically-spaced MNPs with a center-to-center distance d_{nn} . Each QD is at a center-to-center distance d_{qn} from the nearest MNP. We denote the surface-to-surface distance between neighboring MNPs and between each QD

and the nearest MNP by s . The parameters r_0 and r denote the radii of the QD and MNP, respectively. The distances in Fig. 1 are therefore $d_{qn} = r_0 + s + r$, $d_{nn} = s + 2r$, and $d_{qq} = 2(rn + r_0) + s(n+1)$, where n is the number of MNPs in the NA. We set $s = r = 30$ nm, satisfying the *point-dipole approximation* [13, 49]: $d_{qn} \geq 2r$ and $d_{nn} \geq 3r$. The QD and MNP can, therefore, be treated as point dipoles with dipole moments $\mu_1 = \mu_2 = \mu_{QD}\hat{e}_z$ and $\mu_{MNP}\hat{e}_z$, respectively, where \hat{e}_z is a unit vector in the z direction. This approximation allows us to ignore multipolar effects, which usually manifest strongly at coupling distances $s \ll r$ [39].

Following similar plasmon waveguide-mediated entanglement setups where the illuminating field polarization vector is parallel to the long axis of the waveguide [61, 62], we model the QD-NA-QD system as being driven by a z -polarized and time-varying electric field, $\mathbf{E}(t) \approx 2E_0 \cos(\omega t)\hat{e}_z$, propagating in the x direction with a wavevector $\mathbf{k} = k\hat{e}_x$. Here, ω is the driving frequency, $E_0 = (2I/c\sqrt{\epsilon_m}\epsilon_0)^{1/2}$ is the amplitude of the field, with I being the driving field intensity, ϵ_m the dielectric constant of the host medium, c the speed of light in vacuum, and ϵ_0 the free-space permittivity. We have applied the *long-wavelength approximation* [49, 51], since the MNP radius with respect to the propagation distance of light in the x direction is in the Rayleigh regime: $r \ll 2\pi c/\omega$. Note that this approximation breaks down if the light field is polarized in the x direction, since this will result in a propagation wavevector in the z direction where $d_{qq} \gtrsim 2\pi c/\omega \forall n > 1$. Therefore, we do not consider the x -polarized field, since it leads to significant radiation damping due to phase-retardation along the length of the NA.

As shown in Fig. 1, the QD-MNP and the MNP-MNP coupling rates are denoted as g and κ , respectively. The above approximations allow us to consider nearest-neighbor dipole–dipole interactions only, since these coupling rates dominate the interactions at such length scales [51]. In addition, they are small compared to the driving frequency, satisfying the *weak-coupling approximation* [13]: $g, \kappa \ll \omega = \omega_0$, where ω_0 denotes the localized surface plasmon resonance (LSPR) of a single MNP in the NA. Refs. [9, 37–39] have shown how g is derived. A similar approach can be applied to an MNP homodimer (see Appendix A) to obtain κ and μ_{MNP} . Hence, we have the following equations:

$$g = \frac{s_z \mu_{QD}}{d_{qn}^3} \sqrt{\frac{3r^3 \eta}{4\pi \epsilon_0 \hbar}}, \quad (1a)$$

$$\kappa = 3s_z \epsilon_m \eta \left(\frac{r}{d_{nn}^3} \right)^3, \quad (1b)$$

$$\mu_{MNP} = 2\epsilon_m \sqrt{3\pi \epsilon_0 \hbar \eta r^3}, \quad (1c)$$

where $s_z = +2$ is a dipole orientation factor corresponding to longitudinal coupling of the dipole moments involved in each coupling rate, $\mu_{QD} = e r_0$, with e being the electronic charge, $\eta \approx \omega_0/2(\epsilon_\infty + 2\epsilon_m)$, $\omega_0 \approx \omega_p/\sqrt{\epsilon_\infty + 2\epsilon_m}$, with ϵ_∞ and ω_p being the high-frequency permittivity and bulk plasma frequency of the metal, respectively, and \hbar is the Dirac constant.

The coherent part of the system's dynamics is described by

the following Jaynes-Cummings type Hamiltonian:

$$H = H_{QD} + H_{NA} + H_{QD-NA-QD}, \quad (2)$$

where H_{QD} and H_{NA} are the Hamiltonians of the QDs and NA, respectively, and $H_{QD-NA-QD}$ is the interaction Hamiltonian of the QD-NA-QD system. Based on previous works [13, 51, 56], the components of the Hamiltonian in Eq. (2), in a frame rotating with the driving frequency, can be written as

$$H_{QD} = \hbar \sum_{i=1}^2 \left(\Delta\omega_i \sigma_i^\dagger \sigma_i - \Lambda_i (\sigma_i^\dagger + \sigma_i) \right), \quad (3a)$$

$$H_{NA} = \hbar \sum_{m=1}^n \left(\Delta\omega_0 a_m^\dagger a_m - \Omega_m (a_m^\dagger + a_m) \right) - \hbar \sum_{m,v|m < v} \kappa_{mv} (a_m^\dagger a_v + a_m a_v^\dagger), \quad (3b)$$

$$H_{QD-NA-QD} = -\hbar \sum_{m=1}^n \sum_{i=1}^2 g_{im} (\sigma_i^\dagger a_m + \sigma_i a_m^\dagger), \quad (3c)$$

where $\kappa_{mv} = \kappa$ for $v \in \text{ngbb}(m)$ and zero otherwise, $g_{11} = g_{22} = g$, $g_{1(m>1)} = g_{2(m<n)} = 0$ (i.e., only nearest-neighbor QD-MNP couplings are non-zero), $\Delta\omega_i = \omega_i - \omega$ is the detuning of the transition frequency of each QD from the driving frequency, σ_i^\dagger (σ_i) is the raising: $|e_i\rangle\langle g_i|$ (lowering: $|g_i\rangle\langle e_i|$) operator of each QD, $\Lambda_i = E_0 \mu_i / \hbar$ is the excitation rate of each QD, $\Delta\omega_0 = \omega_0 - \omega$ is the detuning of the LSPR of each MNP from the driving frequency, a_m^\dagger (a_m) is the plasmon creation (annihilation) operator of each MNP, and $\Omega_m = E_0 \mu_{MNP} / \hbar$ is the excitation rate of each MNP.

At optical frequencies, the Liouvillian describing the dissipative part of the evolution of the reduced density matrix ρ of the system due to its interaction with the environment, within the Markov approximation [38, 51], is given by

$$L\rho = \frac{1}{2} \sum_{i=1}^2 \gamma_i D_i[\sigma_i, \rho] + \frac{1}{2} \sum_{m=1}^n \gamma_0 D_m[a_m, \rho], \quad (4)$$

where $D_i[\sigma_i, \rho] = 2\sigma_i \rho \sigma_i^\dagger - \{\sigma_i^\dagger \sigma_i, \rho\}$ and $D_m[a_m, \rho] = 2a_m \rho a_m^\dagger - \{a_m^\dagger a_m, \rho\}$ are the dissipators consisting of contributions from the spontaneous emission rate γ_i of the i -th QD qubit and plasmon damping rate γ_0 of the m -th MNP, respectively. The plasmon damping rate, $\gamma_0 = \gamma_{nr} + \gamma_r$, is due to both non-radiative damping, $\gamma_{nr} = \gamma_p (1 + (\gamma_p / \omega_0)^2)$, with γ_p being the damping rate of the free electrons of the metal, and radiative damping, $\gamma_r = \mu_{MNP}^2 \sqrt{\epsilon_m} \omega_0^3 / 3\pi \epsilon_0 \hbar c^3$, of the dipole plasmon [38, 40].

III. EFFECTIVE MODEL

In addition to the weak-coupling approximation, the effective approach used in Refs. [56, 59] and adopted here also requires the system to be driven weakly. In the weak-field limit, $\Omega_m \ll \gamma_0$ (since $\Omega_m \gg \Lambda_i$ and $\gamma_0 \gg \gamma_i$), the joint expectation values of the MNP and QD operators appearing in the equations of motion (EOM) can be factored [38]. To

obtain the EOM, the evolution of the reduced density matrix of the system is described by the Lindblad equation [38, 68]:

$$\dot{\rho} = \frac{i}{\hbar} [\rho, H] + L\rho. \quad (5)$$

Using $\text{tr}(a_m \dot{\rho}) = \langle \dot{a}_m \rangle$ and $\text{tr}(\sigma_i \dot{\rho}) = \langle \dot{\sigma}_i \rangle$, we obtain the following EOM:

$$\langle \dot{a}_m \rangle = -\delta \langle a_m \rangle + i \left(\Omega_m + \sum_v \kappa_{mv} \langle a_v \rangle \right) + \langle \sigma_1 \rangle g_{1m} + \langle \sigma_2 \rangle g_{2m}, \quad (6a)$$

$$\langle \dot{\sigma}_i \rangle = -\delta_i \langle \sigma_i \rangle - i \left(\Lambda_i + \sum_{m=1}^n g_{im} \langle a_m \rangle \right) \langle \sigma_z^i \rangle, \quad (6b)$$

where $\delta = i\Delta\omega_0 + \gamma_0/2$, $\delta_i = i\Delta\omega_i + \gamma_i/2$, $\langle \sigma_z^i \rangle$ is the expectation value of the population difference operator, $\sigma_z^i = 2\sigma_i^\dagger \sigma_i - 1$, of each QD qubit, the expectation values of the MNP and QD fluctuation operators are zero, and joint expectation values have been factored. Since $\gamma_0 \gg \gamma_i$, the MNP dynamics can be treated as stationary with respect to the dynamics of the QD qubits [27, 56, 59]. This enables the expectation value of the MNP annihilation operator to be eliminated adiabatically from the qubit dynamics using the stationary solution of Eq. (6a):

$$\langle a_m(t \rightarrow \infty) \rangle = \frac{i}{\delta} \left(\tilde{\Omega}_m + \tilde{g}_{1m} \langle \sigma_1 \rangle + \tilde{g}_{2m} \langle \sigma_2 \rangle \right), \quad (7)$$

where $\tilde{\Omega}_m = \sum_v K_{mv} \Omega_v$ is the effective excitation rate of each MNP due to the nearest-neighbor MNP-MNP interactions, $\tilde{g}_{1m} = \sum_v g_{1v} K_{mv}$ and $\tilde{g}_{2m} = \sum_v g_{2v} K_{mv}$ are the effective QD-MNP coupling rate of each QD, respectively, and K_{mv} are the elements of the inverse of the coupling matrix $A^{(n)}$ —an $n \times n$ square matrix with diagonal entries $A_{ii}^{(n)} = 1$ and off-diagonal entries $A_{ij}^{(n)} = -i\kappa/\delta$ (for nearest-neighbor interactions) and $A_{ij}^{(n)} = 0$ (otherwise). Substituting Eq. (7) into Eq. (6b) for $\langle a_m \rangle$ leads to

$$\langle \dot{\sigma}_i \rangle = -\tilde{\delta}_i \langle \sigma_i \rangle - i\tilde{\Lambda}_i \langle \sigma_i \rangle - \left(i\tilde{G}_{ij} - \frac{1}{2}\tilde{\Gamma}_{ij} \right) \langle \sigma_z^i \rangle \langle \sigma_j \rangle, \quad (8)$$

with $\tilde{\delta}_i = (i\Delta\omega_i + \frac{1}{2}\tilde{\gamma}_i)$, where the plasmon-induced effects

$$\Delta\tilde{\omega}_i = \Delta\omega_i - \sum_{m=1}^n g_{im} \frac{V_{im}}{|\delta|^2}, \quad (9a)$$

$$\tilde{\gamma}_i = \gamma_i + \sum_{m=1}^n g_{im} \frac{2U_{im}}{|\delta|^2}, \quad (9b)$$

$$\tilde{\Lambda}_i = \Lambda_i + \sum_{m=1}^n g_{im} \frac{i\tilde{\Omega}_m}{\delta}, \quad (9c)$$

are the exciton shift, Purcell enhancement, and excitation rate enhancement, respectively, of the QD qubits, and

$$\tilde{G}_{ij} = \sum_{m=1}^n g_{im} \frac{V_{jm}}{|\delta|^2}, \quad \tilde{\Gamma}_{ij} = \sum_{m=1}^n g_{im} \frac{2U_{jm}}{|\delta|^2}, \quad (10)$$

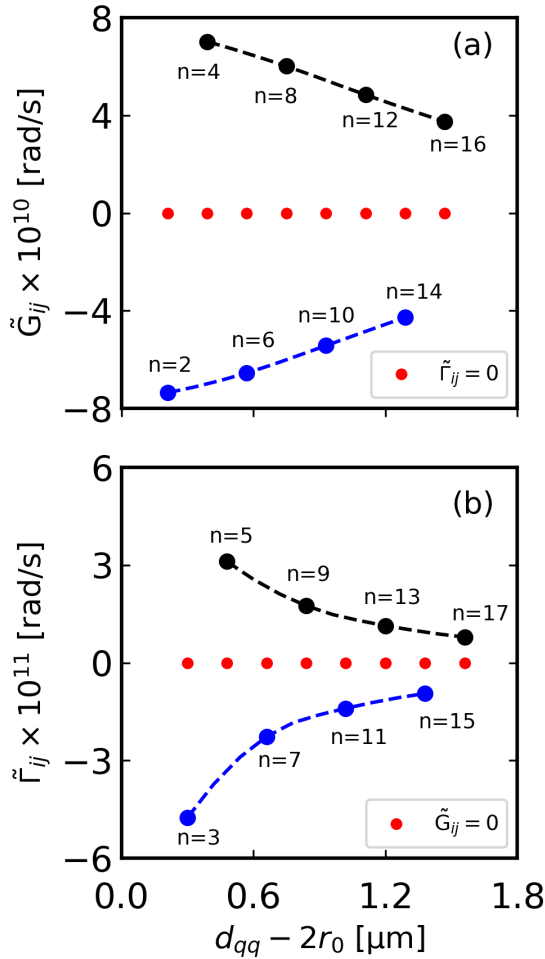


FIG 2. (Color online) Dependence of the coherent coupling, \tilde{G}_{ij} and the dissipative coupling, $\tilde{\Gamma}_{ij}$ ($i = 1, j = 2$), on the inter-qubit separation $d_{qq} - 2r_0$ for (a) even- n arrays: $\tilde{G}_{ij} \neq 0$, $\tilde{\Gamma}_{ij} = 0$ and (b) odd- n arrays: $\tilde{G}_{ij} = 0$, $\tilde{\Gamma}_{ij} \neq 0$, at $\omega = \omega_0 \approx 2\pi c/(480 \text{ nm})$. Dashed curves: polynomial fits. Solid points: data.

are the plasmon-mediated interactions, with matrix elements $V_{jm} = \Delta\omega_m \Re[\tilde{g}_{jm}] - \frac{1}{2} \gamma_0 \Im[\tilde{g}_{jm}]$ and $U_{jm} = \Delta\omega_m \Im[\tilde{g}_{jm}] + \frac{1}{2} \gamma_0 \Re[\tilde{g}_{jm}]$. In Eq. (10), \tilde{G}_{ij} is the coherent coupling rate, responsible for the unitary evolution of the qubits, while their non-unitary dynamics is due to the dissipative coupling rate $\tilde{\Gamma}_{ij}$, and the effective spontaneous emission rate $\tilde{\gamma}$ given by Eq. (9b). Based on Eqs. (9a)-(9c) and (10), and the effective model in Refs. [56, 61], we can write the effective Hamiltonian and Liouvillian of the NA-coupled QD qubits as follows:

$$\tilde{H} = \hbar \sum_{i=1}^2 \left(\Delta\tilde{\omega}_i \sigma_i^\dagger \sigma_i - (\tilde{\Lambda}_i \sigma_i^\dagger + \tilde{\Lambda}_i^* \sigma_i) \right) - \hbar \sum_{i,j=1}^2 G_{ij} (1 - \delta_{ij}) \sigma_i^\dagger \sigma_j, \quad (11a)$$

$$\tilde{L}\rho = \frac{1}{2} \sum_{i,j=1}^2 \tilde{\Gamma}_{ij} (2\sigma_i \rho \sigma_i^\dagger - \{\sigma_i^\dagger \sigma_j, \rho\}). \quad (11b)$$

The NA investigated is that of silver nanoparticles (AgNPs). We assume that each AgNP in the NA is surrounded by a medium of dielectric constant $\epsilon_m \approx 2.98$. This leads to a single particle resonance frequency $\omega_0 \approx 2\pi c/(480 \text{ nm})$, obtained with the following Drude parameters: $\omega_p \approx 8.5472 \text{ eV}$, $\epsilon_\infty \approx 5$ and $\gamma_p = 0.018 \text{ eV}$. Here, ω_p and ϵ_∞ have been adjusted to reproduce typical LSPR values of an AgNP on silicon-based substrates [69]. We consider two similar QD qubits, each with radius $r_0 = 2 \text{ nm}$ (corresponding to $\mu_{QD} \sim 96 \text{ Debye}$), spontaneous emission rate $\gamma_i = 2\pi \times 10^8 \text{ rad/s}$, and a transition frequency $\omega_i \approx \omega_0$, such as tunable cadmium-based core-shell quantum dots [32].

As shown in Fig. 2, the plasmon-mediated couplings in Eq. (10) are affected by the number, n , of MNPs in the NA, at the driving frequency $\omega = \omega_0$ of the single MNP LSPR. Though the coherent coupling, \tilde{G}_{ij} , and the dissipative coupling, $\tilde{\Gamma}_{ij}$, are independent of the driving field intensity, they oscillate as the driving frequency ω is varied, reaching crests or troughs, depending on the value of n . These mediated coupling rates have positive values at the crests and negative values at the troughs. The values displayed in Fig. 2 are for $\omega = \omega_0$, since they are the optimal inter-qubit coupling rates when the QD-NA-QD system is driven resonantly at the single MNP LSPR.

The polynomial fits in Fig. 2 reveal the dependence of the NA-mediated interactions— \tilde{G}_{ij} and $\tilde{\Gamma}_{ij}$ —on the qubit-qubit separation. The fits show that the MNP array waveguide leads to mediated interactions with a nonlinear dependence on the inter-qubit separation, in contrast with certain plasmon waveguides [62], where the mediated interactions have a linear dependence on the inter-qubit distance. Here, both \tilde{G}_{ij} and $\tilde{\Gamma}_{ij}$ are quadratic in $d_{qq} - 2r_0$, but the nonlinearity is more pronounced in $\tilde{\Gamma}_{ij}$, as shown in Fig. 2 (b). This is likely due to differences in the number of hybrid plasmon resonances as well as other factors, such as plasmon damping and qubit-NA interactions at the driving frequency, $\omega = \omega_0$.

When n is even, Fig. 2 (a) shows that the qubits can only interact via coherent coupling (since $\tilde{\Gamma}_{ij} = 0$). This is because the oscillatory behavior of the dissipative coupling in an even- n array is out-of-phase with the driving field at $\omega = \omega_0$, while that of the coherent coupling is in-phase with the field. The converse is the case for odd- n arrays, i.e., the qubits can only interact via dissipative coupling when n is odd (since $\tilde{G}_{ij} = 0$), as shown in Fig. 2 (b).

For certain values of n , the inter-qubit couplings can either attain their crests or troughs at $\omega = \omega_0$. This leads to different n array sequences, each with a common difference of 4, as shown in Fig. 2. The constant common difference arises due to the behavior of the mediated couplings at $\omega = \omega_0$. For instance, a trough in \tilde{G}_{ij} at $n = 2$ is followed by a trough in $\tilde{\Gamma}_{ij}$ at $n = 3$, a crest in \tilde{G}_{ij} at $n = 4$, then a crest in $\tilde{\Gamma}_{ij}$ at $n = 5$, before the next trough in \tilde{G}_{ij} at $n = 6$. The dissipative coupling rate (Fig. 2 (b)) for odd- n arrays is about an order of magnitude greater than the coherent coupling rate (Fig. 2 (a)) for even- n arrays. This is because, unlike even- n arrays, where the hybrid modes are off-resonant, odd- n arrays support a hybridized LSPR at $\omega = \omega_0$, leading to enhanced interaction due to resonant coupling. As n increases, the inter-

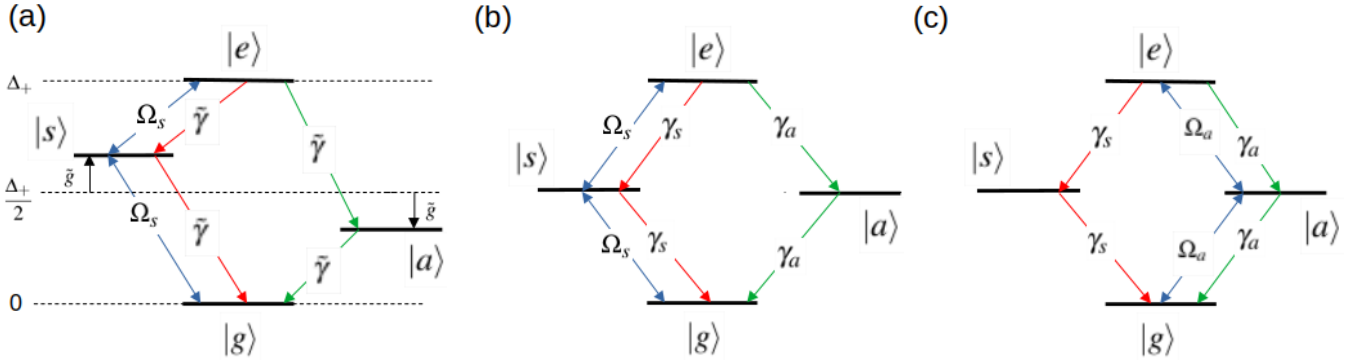


FIG. 3. (Color online) Energy-level diagrams showing the transition rates at the driving frequency $\omega = \omega_0$ between the Dicke states of the two NA-coupled qubits for the (a) even- n array with symmetric excitation rate, Ω_s , (b) odd- n array with symmetric excitation rate, Ω_s , and (c) odd- n array with antisymmetric excitation rate, Ω_a .

qubit distance increases via d_{qq} , causing both $|\tilde{\Gamma}_{ij}|$ and $|\tilde{G}_{ij}|$ to decrease due to their dipole character. As we discuss in the next section, the positive and negative values of $\tilde{\Gamma}_{ij}$ and \tilde{G}_{ij} enable optimal control of the energy levels and transition rates involved in entanglement mediation with the NA.

IV. MEDIATED ENTANGLEMENT

A. Transition rates

It is often useful to discuss the transition rates between the energy levels of the two-qubit states involved in bipartite entanglement in the Dicke basis [11, 27, 56]: $|g\rangle = |0\rangle$, $|s\rangle = \frac{1}{\sqrt{2}}(|1\rangle + |2\rangle)$, $|a\rangle = \frac{1}{\sqrt{2}}(|1\rangle - |2\rangle)$, $|e\rangle = |3\rangle$, where the qubit-qubit Hamiltonian given by Eq. (11a) is diagonal, $|g\rangle$ and $|e\rangle$ are the ground and excited states of the two QD qubits, while $|s\rangle$ and $|a\rangle$ are Bell states, referred to as symmetric and antisymmetric states of the qubits, respectively. Here, explicitly, the states $|0\rangle = |g_1\rangle \otimes |g_2\rangle$, $|1\rangle = |e_1\rangle \otimes |g_2\rangle$, $|2\rangle = |g_1\rangle \otimes |e_2\rangle$, and $|3\rangle = |e_1\rangle \otimes |e_2\rangle$ are in the so-called computational basis [11]. In the following, we transform Eqs. (11a) and (11b) to the Dicke basis using the collective operators: $S = (\sigma_1 + \sigma_2)/\sqrt{2}$ and $A = (\sigma_1 - \sigma_2)/\sqrt{2}$ [27], denoting the symmetric and antisymmetric operators, respectively, to obtain:

$$\tilde{H} = \hbar(E_+ S^\dagger S + E_- A^\dagger A + \Delta_- (S^\dagger A + A^\dagger S)) - \hbar(S^\dagger \Omega_s + A^\dagger \Omega_a + S \Omega_s^* + A \Omega_a^*), \quad (12a)$$

$$\tilde{L}\rho = \frac{\gamma_s}{2}(2S\rho S^\dagger - \{S^\dagger S, \rho\}) + \frac{\gamma_a}{2}(2A\rho A^\dagger - \{A^\dagger A, \rho\}). \quad (12b)$$

In the above, $E_\pm = \left(\frac{\Delta_+}{2} \pm \tilde{g}\right)$, $\tilde{g} = \tilde{G}_{12} = \tilde{G}_{21}$, $\Delta_+ = (\tilde{\Delta}\omega_1 + \tilde{\Delta}\omega_2)/2$, $\Delta_- = (\tilde{\Delta}\omega_1 - \tilde{\Delta}\omega_2)/2$, $\Omega_s = (\tilde{\Lambda}_1 + \tilde{\Lambda}_2)/\sqrt{2}$, $\Omega_a = (\tilde{\Lambda}_1 - \tilde{\Lambda}_2)/\sqrt{2}$, $\gamma_s = \tilde{\gamma} + \tilde{\Gamma}_{12}$, $\gamma_a = \tilde{\gamma} - \tilde{\Gamma}_{12}$, $\tilde{\gamma} = \tilde{\gamma}_1 = \tilde{\gamma}_2$, $\tilde{\Gamma}_{12} = \tilde{\Gamma}_{21}$, $S^\dagger S = |e\rangle\langle e| + |s\rangle\langle s|$, $A^\dagger A = |e\rangle\langle e| + |a\rangle\langle a|$, $S = |g\rangle\langle s| + |s\rangle\langle e|$, and $A = |g\rangle\langle a| - |a\rangle\langle e|$.

Based on Eqs. (12a) and (12b), the energy-level diagrams showing the transition rates between the four Dicke states are

constructed as shown in Fig. 3, for even- n and odd- n NA mediators. When n is even (Fig. 3 (a)), $\tilde{G}_{ij} \neq 0$ and $\tilde{\Gamma}_{ij} = 0$ at $\omega = \omega_0$, so that $E_+ \neq E_-$ and $\gamma_s = \gamma_a = \tilde{\gamma}$, respectively, i.e., the energy levels of the symmetric and antisymmetric states split while their decay rates remain the same. Figs. 4 (a)-(d) further show why this is the case for the decay rates when n is even. Here, the hybrid plasmon modes of the NA split into n modes, which are symmetric around the driving frequency. The modes contribute to the symmetric and antisymmetric decay rates, γ_s and γ_a , of the coupled qubits. For instance, when $n = 2$ (Fig. 4 (a)), the hybridized plasmon resonance splits into two single modes, each contributing to either one of the decay rates—the higher-energy mode ($\omega > \omega_0$) contributes to γ_s (red curve), while γ_a (green curve) is due to a lower-energy mode ($\omega < \omega_0$). As n increases, the number of higher- and lower-energy modes contributing to the decay rates increases. This is shown in Figs. 4 (b)-(d). For example, when $n = 4$ (Fig. 4 (b)), the hybridized modes split into two dimer modes, each contributing to the decay rates.

However, as shown in Figs. 4 (a)-(d), the mode splitting is such that the two decay rates coincide at the driving frequency, $\omega = \omega_0$. Hence, when n is even, the symmetric and antisymmetric states, $|s\rangle$ and $|a\rangle$, will decay to the ground state, $|g\rangle$, at the same rate—the effective spontaneous emission rate, $\tilde{\gamma}$, of the qubit—while the bi-excited state, $|e\rangle$, will decay to $|g\rangle$ at the rate $2\tilde{\gamma}$, as illustrated in Fig. 3 (a). Figs. 4 (a)-(d) show that as n increases, $\tilde{\gamma}$ increases at $\omega = \omega_0$, making the system more lossy and the even- n array less efficient as an entanglement mediator, through an enhanced decay to the ground state via $\tilde{\gamma}$. In addition, since $\tilde{g} = \tilde{G}_{ij}$, the energy level of the symmetric state, shown in Fig. 3 (a), undergoes either an upward or a downward shift while that of the antisymmetric state shifts downward or upward, depending on the sequence of the even- n array mediating the qubit-qubit interaction.

To optimize entanglement mediation with the even- n array, the qubits are driven symmetrically and detuned symmetrically from the single-particle LSPR, ω_0 . Symmetric driving via $\tilde{\Lambda}_1 = \tilde{\Lambda}_2$, results in $\Omega_s \neq 0$ and $\Omega_a = 0$, giving the energy-level diagram shown in Fig. 3 (a). This allows the symmetric state population, ρ_{ss} , to contribute most to the degree of stationary entanglement when n is even. The qubit

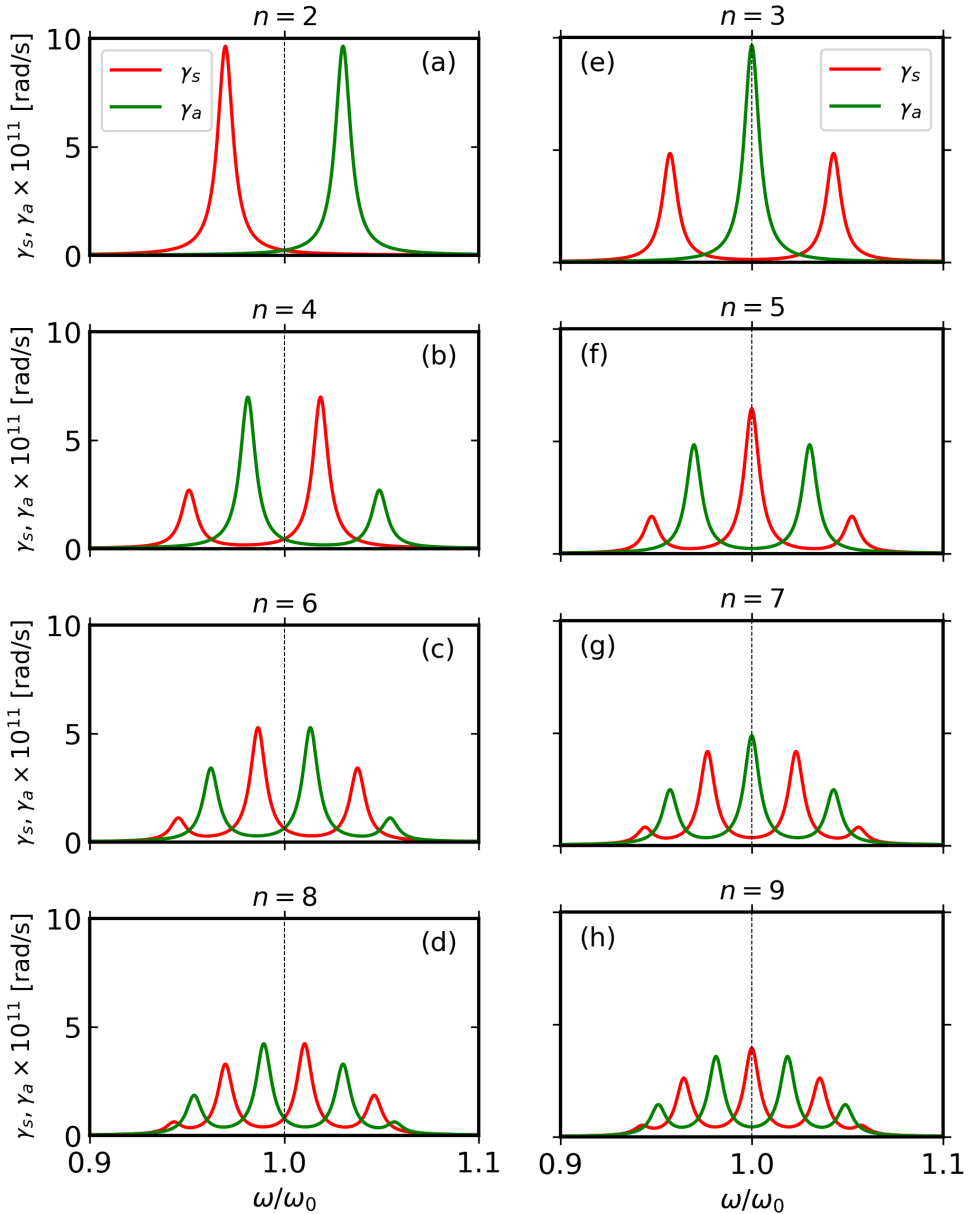


FIG 4. (Color online) Symmetric and antisymmetric decay rates, γ_s and γ_a , as a function of the driving frequency ω for even- n arrays: $n = 2, 4, 6, 8$ and odd- n arrays: $n = 3, 5, 7, 9$. The dashed vertical line in each panel represents the position of the single particle LSPR, ω_0 .

detunings are chosen such that when \tilde{g} is positive, the amount of detuning, $\Delta_1 = \Delta_2 = \Delta$, for each qubit (via $\omega_1 = \omega_0 + \Delta_1$ and $\omega_2 = \omega_0 + \Delta_2$), is also positive, and vice versa, leading to $\Delta_+ = \pm 2\Delta$, $\Delta_- = 0$, and $E_{\pm} = +\Delta \pm |\tilde{g}|$ for positive \tilde{g} ($n = 4, 8, 12, \dots$) and $E_{\pm} = -\Delta \mp |\tilde{g}|$ for negative \tilde{g} ($n = 2, 6, 10, \dots$). The term involving Δ_- , which couples $|s\rangle$ to $|a\rangle$ is therefore not present in Eq. (12a), further facilitating the build up of ρ_{ss} . As we explain in more detail in the next section, the value of Δ is chosen such that it has a similar order of magnitude as \tilde{g} , otherwise the role of \tilde{g} in tuning the energy levels of $|e\rangle$, $|s\rangle$ and $|a\rangle$ becomes insignificant.

When n is odd, $\tilde{G}_{ij} = 0$ at $\omega = \omega_0$, hence there is no shift in the energy levels of the symmetric and antisymmetric states, i.e., $E_+ = E_-$, as illustrated in Figs. 3 (b) and (c).

However, as shown in Figs. 4 (e)-(h), the mode splitting behavior of the hybridized plasmon modes in the symmetric and antisymmetric decay rates of the qubits is such that, while the splitting still consists of n plasmon resonances, the splitted modes contribute unequally to the symmetric and antisymmetric decay rates of the odd n -array coupled qubits. For instance, when $n = 3$ (Fig. 4 (e)), a hybrid single mode at $\omega = \omega_0$ is responsible for the antisymmetric decay rate (green curve), while the symmetric decay rate is due to a hybrid dimer mode (red curve), consisting of both higher- and lower-energy modes. This is because when $n = 3$, $\tilde{\Gamma}_{ij}$ is negative, which leads to $\gamma_a > \gamma_s$ at $\omega = \omega_0$, corresponding to the LSPR of the hybrid single mode. However, when $n = 5$, $\tilde{\Gamma}_{ij}$ is positive, leading to $\gamma_s > \gamma_a$ at $\omega = \omega_0$, and so

on. Therefore, this switching behavior, from $\gamma_a > \gamma_s$ to $\gamma_s > \gamma_a$ and back, follows the same odd n -array sequences that are identified in the mediated interactions shown in Fig. 2. Thus, depending on the number of particles in the odd- n array, the symmetric state, $|s\rangle$, becomes the subradiant state, while the antisymmetric state, $|a\rangle$, will be superradiant, and vice versa. As n increases, Figs. 4 (e)-(h) show that $|\gamma_a - \gamma_s|$ decreases at $\omega = \omega_0$, which is a result of a weakening of the dissipative coupling, since $|\gamma_a - \gamma_s| = 2|\tilde{\Gamma}_{ij}|$.

In the odd- n array mediators, the qubits are not detuned from the single MNP LSPR ($\Delta_1 = \Delta_2 = 0$, so that we have $\Delta_- = 0$ again); rather, the mediated entanglement is optimized via the symmetric and antisymmetric decay and excitation rates. This allows either the symmetric or antisymmetric state population to contribute most to the degree of entanglement, depending on the odd n -array sequence. When $\gamma_a > \gamma_s$ ($n = 3, 7, 11, \dots$), we drive the qubits symmetrically ($\Omega_s \neq 0, \Omega_a = 0$) as shown in Fig. 3 (b), so that the population of the symmetric state, $|s\rangle$, which is the slowly-decaying state in this case, is optimized over that of $|a\rangle$ for entanglement generation. On the other hand, in Fig. 3 (c), the qubits are driven antisymmetrically ($\Omega_s = 0, \Omega_a \neq 0$), since $|a\rangle$ is the subradiant state in this case ($\gamma_s > \gamma_a$ for $n = 5, 9, 13, \dots$), allowing a higher population, ρ_{aa} , of the antisymmetric state in the degree of entanglement, compared to ρ_{ss} . Assuming that two laser fields are used to drive the qubits such that $\tilde{\Lambda}_2 = \tilde{\Lambda}_1 e^{i\phi}$, with ϕ being a phase difference between the two fields, symmetric excitation is realized by a phase difference of $\phi = 0$, while antisymmetric excitation is achieved by setting $\phi = \pi$, resulting in a phase shift of π radians between the two laser fields [10, 62].

B. Stationary concurrence

We calculate the degree of entanglement generated in the two-qubit system using the concurrence [3]

$$C = \max \left(0, \lambda_1 - \sum_{i>1} \lambda_i \right), \quad (13)$$

with λ_i being the eigenvalues in descending order of the matrix $\sqrt{\rho \tilde{\rho} \sqrt{\rho}}$, with $\tilde{\rho} = (\sigma_y \otimes \sigma_y) \rho^* (\sigma_y \otimes \sigma_y)$, where ρ^* is the complex conjugate of ρ and σ_y is the Pauli Y matrix, and $0 < C < 1$ for partially entangled states [11]. To obtain the elements of the steady-state density matrix, $\rho^{ss} \equiv \rho(t \rightarrow \infty)$, of the two-qubit system, Eq. (5) was solved in the computational basis at $t \rightarrow \infty$ with both H and L replaced with their effective versions given by Eq. (11a) and Eq. (11b), respectively. The solution is too lengthy to be written out here in its entirety, so we write it in component form as follows:

$$\rho_k^{ss} = \sum_{l=1}^{16} (M^{-1})_{kl} B_l, \quad k = 1, 2, \dots, 16 \quad (14)$$

where $\rho_k^{ss} = [\rho_{ii}|_{i=0}^3, \Re \rho_{ij}|_{0 \leq i < j \leq 3}, \Im \rho_{ij}|_{0 \leq i < j \leq 3}]^\top$ and $B_l = [1, 0, 0, \dots, 0]^\top$ are 16×1 column vectors, and M is a 16×16 evolution matrix, comprising the effective detuning, damping,

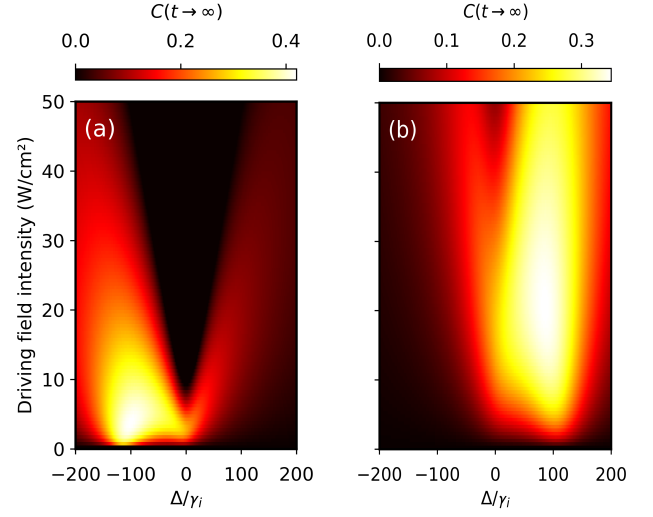


FIG 5. (Color online) Dependence of the stationary concurrence on the driving field intensity and the normalized detuning rate, Δ/γ_i , of each qubit, for the even- n arrays (a) $n = 2$ and (b) $n = 4$.

coupling, and driving terms of the two-qubit system. Here, we have considered I values in the range $0 - 80 \text{ W/cm}^2$, which falls in the weak-excitation regime, $\Omega_m/\gamma_0 \approx 0 - 0.096$.

In order to determine the detuning rate, Δ , of each qubit needed to optimize the mediated entanglement with the even- n arrays, we investigated the dependence of the stationary concurrence, $C(t \rightarrow \infty)$, on values of Δ ranging from $-200\gamma_i$ to $200\gamma_i$ for the range of driving field intensities given above, as shown in Fig. 5. Fig. 5 (a) shows that $C(t \rightarrow \infty)$ is maximized for $n = 2$ when $\Delta \sim -70\gamma_i$ to $-100\gamma_i$, i.e., negative detunings. This is the case for the even- n array sequence $n = 2, 6, 10, \dots$. On the other hand, Fig. 5 (b) shows that $C(t \rightarrow \infty)$ is maximized for $n = 4$ when $\Delta \sim 70\gamma_i$ to $100\gamma_i$, i.e., positive detunings. This is also the case for the even- n array sequence $n = 4, 8, 12, \dots$.

Based on the stationary populations of the Dicke states in our model, we observed that these values of Δ optimize ρ_{ss} over ρ_{aa} , ρ_{ee} , and ρ_{gg} , for entanglement generation mediated by even- n arrays. We propose that this is because these values of Δ are within the same order of magnitude as the coherent coupling rate ($\sim 10^{10} \text{ rad/s}$) shown in Fig. 2 (a). Therefore, we only consider qubit detunings, Δ , for which $|\Delta| \approx |\tilde{g}|$. For the even- n array sequence $n = 2, 6, 10, \dots$, some negative detunings in Fig. 5 (a) satisfy this condition, since $\tilde{g} = \tilde{G}_{ij} < 0$, as shown in Fig. 2 (a), while for the even- n array sequence $n = 4, 8, 12, \dots$, the condition is met via some positive detunings in Fig. 5 (b), since $\tilde{g} = \tilde{G}_{ij} > 0$, as shown in Fig. 2 (a).

Fig. 6 shows the dependence of the stationary concurrence on the driving field intensity. We have set $\Delta = \pm 80\gamma_i$ ($\sim \pm 4.4 \times 10^{10} \text{ rad/s}$), which is within the optimal range of Δ values for the stationary concurrence shown in Fig. 5. As shown in Fig. 6 (a), the concurrence for each even- n array reaches a maximum value at a certain driving field intensity, beyond which it decreases with increasing intensity. Since $C \approx \max(0, \sqrt{(\rho_{ss} - \rho_{aa})^2 + 4\Im \rho_{sa}^2} - 2\sqrt{\rho_{gg} \rho_{ee}})$, with

ρ_{ee} , ρ_{gg} , ρ_{ss} , ρ_{aa} , and ρ_{sa} being the populations of $|e\rangle$, $|g\rangle$, $|s\rangle$, $|a\rangle$, and the coherence between $|s\rangle$ and $|a\rangle$, respectively [11, 56], we observed from our model that the decrease in concurrence with an increase in the field intensity is due to an increase in the population, ρ_{ee} , of the bi-excited state, and a decrease in the populations, ρ_{aa} , ρ_{ss} , and ρ_{gg} while $\Im\rho_{sa} = 0$.

When the qubit–qubit interactions are mediated by the even n -array sequence $n = 2, 6, 10, \dots$ (solid curves in Fig. 6 (a)), the optimal concurrence is attained at weaker driving fields ($I \propto n$) compared to mediation with the even n -array sequence $n = 4, 8, 12, \dots$ (dashed curves in Fig. 6 (a)), where the optimal driving field is $\gtrsim 20$ W/cm². We attribute this to the behavior of $|\Omega_s|$ and $\gamma_s = \tilde{\gamma}_i$ at $\omega = \omega_0$. For instance, $|\Omega_s|(n=2) > |\Omega_s|(n=4)$, and $\gamma_s(n=4) > \gamma_s(n=2)$, so that a higher intensity is required to overcome both the weaker excitation rate and higher damping, and attain an optimal concurrence with $n = 4$. This trend re-occurs in the even n -array pair $n = 6, 8$, and so on. As n increases in each even n -array sequence, the symmetric decay rate, $\gamma_s = \gamma_a = \tilde{\gamma}$, is enhanced via an increase in the spontaneous emission rate, $\tilde{\gamma}_i$, of each qubit, as shown in Figs. 4 (a)-(d), while the energy gap $|E_+ - E_-| = 2|\tilde{G}_{ij}| \rightarrow 0$ at $\omega = \omega_0$. The evolution of populations and coherences in our model shows that this leads to higher values of ρ_{gg} and lower values of ρ_{ee} , ρ_{ss} , ρ_{aa} , while $\Im\rho_{sa} = 0$. As a result, the concurrence decreases.

Fig. 6 (b) shows that the degree of stationary qubit–qubit entanglement is not only preserved but also slightly enhanced in longer NAs via odd n -array mediators compared to even ones. The enhancement comes from either zero values or slightly lower values of ρ_{ee} in comparison to the even n -array mediators, depending on the odd n -array sequence. The optimal concurrence at $\omega = \omega_0$ follows the two sequences previously identified in the dissipative coupling shown in Fig. 2. With the NA sequence $n = 3, 7, 11, \dots$ (solid curves in Fig. 6 (b)), the concurrence reaches an optimal value at a certain intensity ($40 \lesssim I \lesssim 60$ W/cm²), beyond which it increases only slightly ($n = 3$ and $n = 7$) or decreases ($n = 11$ and $n = 15$) with increasing field intensity between 56 W/cm² and 80 W/cm². A further increase in the driving field intensity beyond 100 W/cm² (figure not shown) eventually leads to a decrease in the concurrence for $n = 3$ and $n = 7$, due to an increase in ρ_{ee} , but this is already approaching the strong driving regime, where the validity of the effective model remains questionable [56].

However, with the NA sequence $n = 5, 9, 13, \dots$ (dashed curves in Fig. 6 (b)), ρ_{aa} contributes most to the degree of entanglement, due to dissipative coupling to $|a\rangle$ via $\gamma_a > \gamma_s$, combined with $\Omega_s = 0, \Omega_a \neq 0$, but there are non-zero values of other populations contributing to the entanglement. Hence, in this case, the concurrence peaks at smaller field intensities ($\lesssim 3$ W/cm²), as shown in Fig. 6 (b) (dashed curves). The weaker driving fields required to reach the optimal concurrence with the NA sequence $n = 5, 9, 13, \dots$ in comparison to the sequence $n = 3, 7, 11, \dots$, in Fig. 6 (b), can be explained based on the behavior of $|\Omega_s|$ and $|\Omega_a|$, as well as γ_s and γ_a . For instance, at $\omega = \omega_0$, $|\Omega_s|(n=3) < |\Omega_a|(n=5)$ and $\gamma_a(n=3) > \gamma_s(n=5)$, so that a higher field intensity is required to overcome the increased damping and reach the

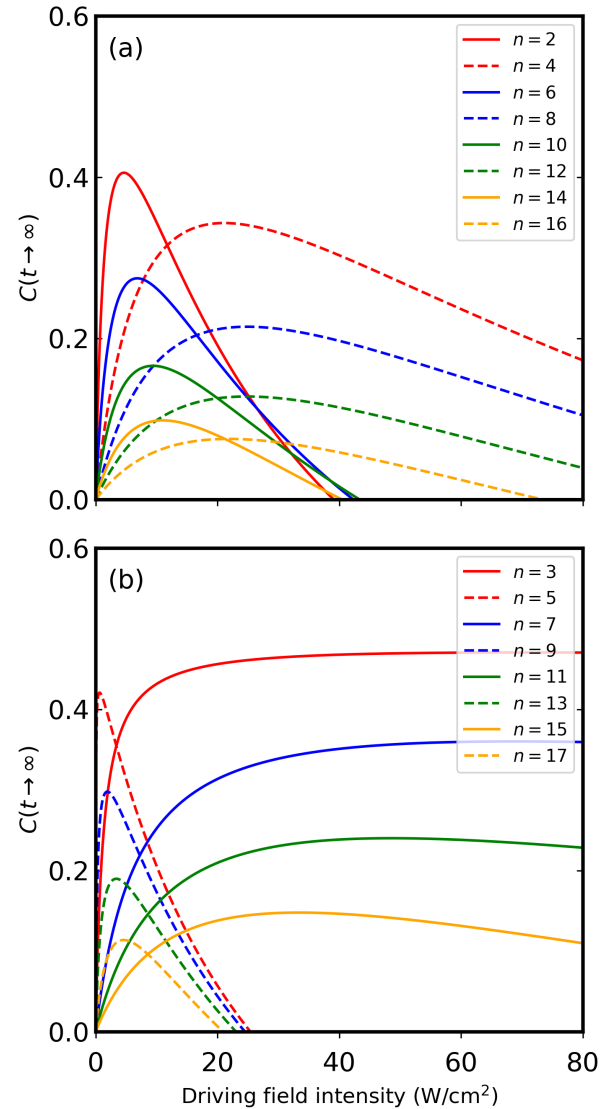


FIG 6. (Color online) Dependence of the stationary concurrence on the intensity of the driving field for (a) even- n arrays $n = 2, 6, 10, 14$ (solid curves) and $n = 4, 8, 12, 16$ (dashed curves), and (b) odd- n arrays $n = 3, 7, 11, 15$ (solid curves) and $n = 5, 9, 13, 17$ (dashed curves). For each n -array mediator, the concurrence has been optimized based on the energy-level diagrams in Fig. 3.

optimal concurrence when $n = 3$. This repeats for the next odd- n pair $n = 7, 9$, and so on. The enhanced excitation rates of the qubits when $n = 5, 9, 13, \dots$ are due to the presence of a hybrid plasmon mode with the same frequency as the single MNP LSPR in the excitation spectrum at $\omega = \omega_0$, i.e., the sequence $n = 5, 9, 13, \dots$, experiences a resonant excitation while the sequence $n = 3, 7, 11, \dots$ undergoes an off-resonant excitation. As n increases, the decay splitting $|\gamma_a - \gamma_s| = 2|\tilde{G}_{ij}| \rightarrow 0$, as shown in Figs. 4 (e)-(h), in each odd n -array sequence. The stationary populations show that this leads to an increase in ρ_{gg} and a decrease in ρ_{ee} , ρ_{ss} , and ρ_{aa} , causing a decrease in the concurrence.

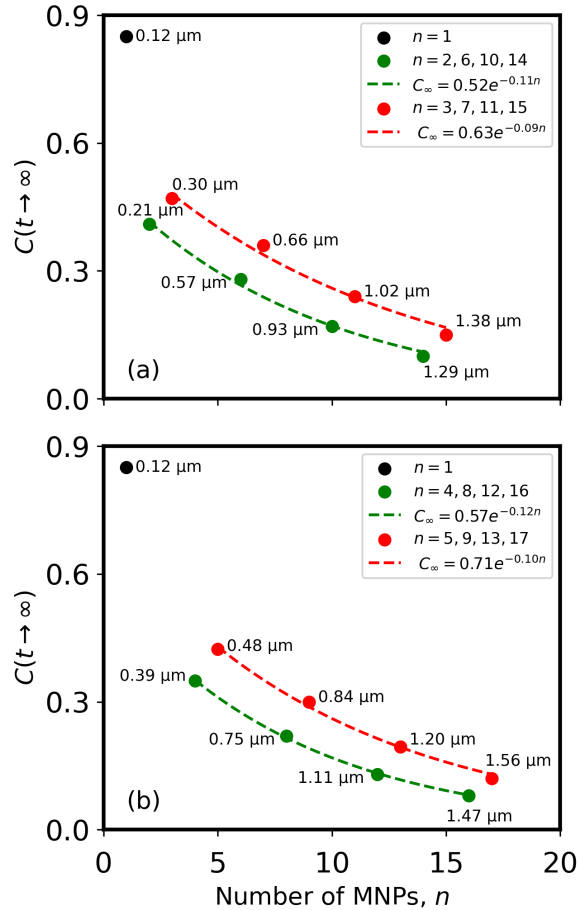


FIG 7. (Color online) Decay of stationary concurrence with increase in the number, n , of MNPs in the array. (a) NA sequences: $n = 2, 6, 10, 14$ and $n = 3, 7, 11, 15$. (b) NA sequences: $n = 4, 8, 12, 16$ and $n = 5, 9, 13, 17$. The inter-qubit distance, corresponding to the number of MNPs in each NA via $d_{qq} - 2r_0 = 2rn + s(n+1)$, is indicated in μm . Solid points: data. Dashed lines: decay fits.

C. Entanglement decay

We now compare the stationary concurrence for even and odd n -array mediators, obtained at $\omega = \omega_0$, based on the optimal driving field intensities discussed in the previous section. Fig. 7 shows the dependence of the concurrence on the number of MNPs, n , in the NA. To serve as a reference, we have included the optimal stationary concurrence obtained for $n = 1$, based on antisymmetric detuning of the qubits, as has been extensively studied in previous works [12, 56, 57, 59]. When $n = 1$, the concurrence is very high ($C_\infty \approx 0.85$), but the inter-qubit distance is very short ($d_{qq} - 2r_0 = 0.12 \mu\text{m}$), as shown in Fig. 7. However, a single MNP is inefficient in long-range entanglement mediation because the initially high concurrence rapidly decays with an increase in the MNP-QD separation. The fitted curves—dashed lines in Fig. 7—show that the stationary concurrence follows a decay law of the form $C_\infty = C_0 e^{-\tau n}$, where τ is the decay constant of stationary concurrence per MNP in the array. In the limit of very long arrays ($n \rightarrow \infty$), we find that the entanglement vanishes, since $C_\infty \rightarrow 0$.

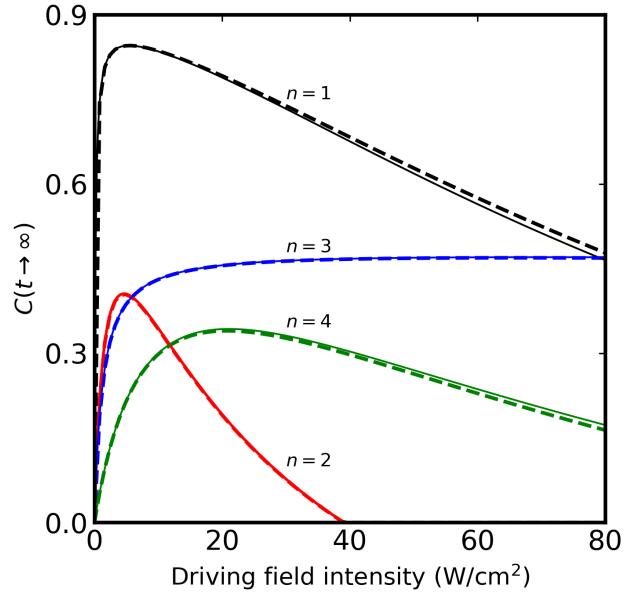


FIG 8. (Color online) Effective model (solid curves) versus simulation (dashed curves) of the mediated stationary concurrence for $n = 1, 2, 3$, and 4 .

$$C_\infty \rightarrow 0.$$

Fig. 7 (a) shows that the odd n -array mediators (red curve) not only sustain the degree of entanglement at longer inter-qubit distances—90 nm greater than those of a neighboring even- n array—but also support a slightly higher degree of entanglement. This trend persists even in longer arrays, as shown in Fig. 7 (b). We attribute the robustness of the odd n -array mediators to entanglement decay ($C_0^{\text{odd } n} > C_0^{\text{even } n}$ and $\tau_{\text{odd } n} < \tau_{\text{even } n}$), to the enhanced dissipative coupling in comparison to the coherent coupling ($\tilde{\Gamma}_{ij} \approx 10 \tilde{G}_{ij}$ at the driving frequency $\omega = \omega_0$, as shown in Fig. 2). For this reason, the decay splitting $|\gamma_a - \gamma_s| = 2|\tilde{\Gamma}_{ij}|$ for odd n is large (Fig. 4 (e)-(h)), and therefore more effective than the energy splitting $|E_a - E_s| = 2|\tilde{G}_{ij}|$ for even n in trapping a higher population of the NA-coupled qubits in either the symmetric or antisymmetric state. Hence, with NAs, the inter-particle coupling, κ , enables the concurrence to be sustained over long inter-qubit distances (μm regime), in contrast to a single MNP where the entanglement decay with an increase in the inter-qubit separation is much more rapid.

D. Model validation

We validated the effective model of the NA-mediated stationary entanglement based on simulations performed using the Quantum Optics Toolbox in Python (QuTiP) [70]. The QuTiP simulations were set up using the total Hamiltonian and Liouvillian given by Eqs. (2) and (4), respectively, to obtain the steady-state density matrix of the coupled system. The concurrence was then calculated using a density matrix of the qubits—a reduced density matrix obtained by performing a partial trace on the steady-state density matrix. Fig. 8 shows

a comparison between the stationary concurrence simulated in QuTiP and calculated analytically using the effective model. There is good agreement between the simulation and the effective model for $n = 1, 2, 3$, and 4.

Here, we have only shown the simulated stationary concurrence up to $n = 4$, but the concurrence due to higher values of n can also be simulated. However, the dimension of the Hilbert space required to perform the simulation is proportional to $2^2(\text{QD qubits}) \times N^n(\text{MNPs})$, where each MNP is modeled as a quantum harmonic oscillator (QHO) with levels $N \geq 2$, representing at least the ground and first excited state of the QHO. To improve the accuracy of the simulated results shown in Fig. 8, we have used $N = 4$. Hence, as n increases, more computational time and memory are needed to simulate the concurrence compared to the effective approach. The effective model, therefore, offers additional benefits beyond providing an in-depth theoretical insight into the behavior of the mediated interactions.

V. CONCLUSION

We have investigated the plasmonic mediation of stationary entanglement in two QD qubits using an effective cavity quantum electrodynamic approach. This has allowed us to obtain a comprehensive insight into the role of plasmon-mediated interactions in long-range entanglement mediation with one-dimensional plasmonic nanoarrays. Within the weak-coupling and weak-excitation limits, the effective model has enabled us to predict MNP number-dependent mediated interactions—coherent and dissipative coupling rates—due to even and odd n -array mediators of the two-qubit entanglement. We found that with even- n arrays, the mediated entanglement is due to the coherent coupling \tilde{G}_{ij} , while the dissipative coupling $\tilde{\Gamma}_{ij}$ is responsible for the degree of entanglement obtained with odd- n arrays. This enables the mediated qubit–qubit entanglement to be optimized via energy splitting ($|E_a - E_s| = 2|\tilde{G}_{ij}|$) when n is even or via decay splitting ($|\gamma_a - \gamma_s| = 2|\tilde{\Gamma}_{ij}|$) when n is odd. Through resonant driving at the single MNP LSPR, the dissipative coupling undergoes a resonant enhancement that enables odd- n arrays to outperform even- n arrays as entanglement mediators.

One might expect the mediated entanglement to decay straightforwardly with increasing number of MNPs in the array but this is not the case. Rather, the entanglement decay inherits the same MNP array sequences found in the mediated interactions. Although the nanoarrays suffer from high ohmic losses and increased weakening of the mediated interactions, which subsequently lead to entanglement decay, we have shown that the proposed scheme is capable of sustaining non-vanishing stationary two-qubit entanglement beyond a qubit–qubit distance of one micron. This decaying entanglement can be distilled [71, 72] or stabilized [14, 66] for use in a quantum information protocol, such as quantum sensing [73–77].

ACKNOWLEDGEMENTS

This research was financially supported by the Department of Science, Technology and Innovation (DSTI) through the South African Quantum Technology Initiative (SA QuTI), Stellenbosch University (SU), the National Research Foundation (NRF), and the Council for Scientific and Industrial Research (CSIR).

Appendix A: Derivation of κ and μ_{MNP}

Consider an MNP homodimer consisting of two MNPs, each of which is treated as a point dipole with dipole moment $\mu_{\text{MNP}}\hat{e}_z$, interacting through the coupling rate κ . The dimer is driven by a z -polarized electric field. We will use the approach in Refs. [9, 37], which involves comparing induced electric fields from quantum and semiclassical formulations.

Let us first obtain the induced electric field on one MNP due to the other MNP in the homodimer in the quantum picture (QP). Based on previous work [51], the Hamiltonian of the driven homodimer in the rotating frame can be written as: $H = \sum_{i=1}^2 \hbar \Delta \omega_i a_i^\dagger a_i - \hbar \kappa (a_1^\dagger a_2 + a_1 a_2^\dagger) - \hbar \Omega \sum_{i=1}^2 (a_i^\dagger + a_i)$. Using the Heisenberg equation of motion, $\langle \dot{a}_1 \rangle = i \langle [H, a_1] \rangle / \hbar + \gamma_1 \langle D(a_1) \rangle / 2$, leads to the stationary solution: $\langle a_1(t \rightarrow \infty) \rangle = i(\Omega + \kappa \langle a_2 \rangle) / \delta_1$, with $\delta_1 = \delta_2 = \delta = i\Delta\omega_0 + \frac{1}{2}\gamma_0$, where $\omega_1 = \omega_2 = \omega_0$ and $\gamma_1 = \gamma_2 = \gamma_0$. The electric field induced by MNP 1 on MNP 2 is obtained as

$$E_{\text{ind}}^{(\text{QP})} = \frac{\hbar \kappa}{\mu_{\text{MNP}}} \langle a_1(t \rightarrow \infty) \rangle = i \frac{\kappa}{\delta} \left(E_0 + \frac{\hbar \kappa \langle a_2 \rangle}{\mu_{\text{MNP}}} \right). \quad (\text{A1})$$

In the semiclassical picture (SCP), we make use of the dipole polarizability [9, 40], $\alpha_1 = \alpha_2 = \alpha = 12i\pi\epsilon_0\epsilon_m^2 r^3 \eta / \delta$, of each MNP in the homodimer. The dipole moment of each MNP is $p_1 = p_2 = \alpha E_{\text{loc}}^{(1)} = \alpha E_{\text{loc}}^{(2)}$, where $E_{\text{loc}}^{(1)} = E_0 + E_{\text{ind}}^{(1)}$ and $E_{\text{loc}}^{(2)} = E_0 + E_{\text{ind}}^{(2)}$ are the respective local fields of the MNPs. In the homodimer, the induced field on each MNP is $E_{\text{ind}}^{(1)} = E_{\text{ind}}^{(2)} = s_z p_2 / 4\pi\epsilon_0\epsilon_m d_{nn}^3$, so that in the SCP we have

$$E_{\text{ind}}^{(\text{SCP})} = \frac{i s_z \epsilon_m r^3 \eta / d_{nn}^3}{\delta} \left(E_0 + \frac{s_z \mu_{\text{MNP}} \langle a_2 \rangle}{4\pi\epsilon_0\epsilon_m d_{nn}^3} \right), \quad (\text{A2})$$

where $E_{\text{ind}}^{(\text{SCP})}$ is the field induced by MNP 1 on MNP 2, and we have replaced p_2 with the QP formulation: $p_2 = \mu_{\text{MNP}} \langle a_2 \rangle$.

Comparing Eq. (A1) to Eq. (A2) leads to

$$\kappa = 3s_z\epsilon_m\eta \left(\frac{r}{d_{nn}^3} \right)^3 = \frac{s_z\mu_{\text{MNP}}}{d_{nn}^3} \sqrt{\frac{3r^3\eta}{4\pi\epsilon_0\hbar}}, \quad (\text{A3a})$$

$$\mu_{\text{MNP}} = 2\epsilon_m \sqrt{3\pi\epsilon_0\hbar\eta r^3}. \quad (\text{A3b})$$

[1] S Luo. Quantum discord for two-qubit systems. *Phys. Rev. A*, 77(4):042303, 2008.

[2] S Virzì, E Rebufello, A Avella, F Piacentini, M Gramegna,

I Ruo Berchera, I. P Degiovanni, and M Genovese. Optimal estimation of entanglement and discord in two-qubit states. *Sci. Rep.*, 9(1):3030, 2019.

[3] W. K Wootters. Entanglement of formation of an arbitrary state of two qubits. *Phys. Rev. Lett.*, 80(10):2245, 1998.

[4] W Dür, G Vidal, and J. I Cirac. Three qubits can be entangled in two inequivalent ways. *Phys. Rev. A*, 62(6):062314, 2000.

[5] D-D Dong, G-B Wei, X-K Song, D Wang, and L Ye. Unification of coherence and quantum correlations in tripartite systems. *Phys. Rev. A*, 106(4):042415, 2022.

[6] K Bedingfield, B Yuen, and A Demetriadou. Subradiant entanglement in plasmonic nanocavities. *Phys. Rev. B*, 111(7):075420, 2025.

[7] I Kogias, A. R Lee, S Ragy, and G Adesso. Quantification of gaussian quantum steering. *Phys. Rev. Lett.*, 114(6):060403, 2015.

[8] Y Xiang, S Cheng, Q Gong, Z Ficek, and Q He. Quantum steering: practical challenges and future directions. *PRX Quantum*, 3(3):030102, 2022.

[9] A Ridolfo, O Di Stefano, N Fina, R Sajja, and S Savasta. Quantum plasmonics with quantum dot-metal nanoparticle molecules: influence of the fano effect on photon statistics. *Phys. Rev. Lett.*, 105(26):263601, 2010.

[10] A Gonzalez-Tudela, D Martin-Cano, E Moreno, L Martin-Moreno, C Tejedor, and F. J Garcia-Vidal. Entanglement of two qubits mediated by one-dimensional plasmonic waveguides. *Phys. Rev. Lett.*, 106(2):020501, 2011.

[11] R Tanaś and Z Ficek. Entangling two atoms via spontaneous emission. *J. Opt. B: Quantum Semiclassical Opt.*, 6(3):S90, 2004.

[12] Y He and K-D Zhu. Strong coupling among semiconductor quantum dots induced by a metal nanoparticle. *Nanoscale Res. Lett.*, 7(1):95, 2012.

[13] C Lee, M Tame, C Noh, J Lim, S. A Maier, J Lee, and D. G Angelakis. Robust-to-loss entanglement generation using a quantum plasmonic nanoparticle array. *New J. Phys.*, 15(8):083017, 2013.

[14] A Irfan, M Yao, A Lingenfelter, X Cao, A. A Clerk, and W Pfaff. Loss resilience of driven-dissipative remote entanglement in chiral waveguide quantum electrodynamics. *Phys. Rev. Res.*, 6(3):033212, 2024.

[15] H Wang, S Liu, and J He. Thermal entanglement in two-atom cavity QED and the entangled quantum otto engine. *Phys. Rev. E*, 79(4):041113, 2009.

[16] C Lee, F Dieleman, J Lee, C Rockstuhl, S. A Maier, and M Tame. Quantum plasmonic sensing: Beyond the shot-noise and diffraction limit. *ACS Photonics*, 3:992–999, 2016.

[17] M Crespi, M Lobino, J. C. F Matthews, A Politi, C. R Neal, R Ramponi, R Osellame, and J. L O’Brien. Measuring protein concentration with entangled photons. *Appl. Phys. Lett.*, 100(23), 2012.

[18] M. A Taylor, J Janousek, V Daria, Knittel, J, B Hage, H-A Bachor, and W. P Bowen. Biological measurement beyond the quantum limit. *Nat. Phot.*, 7(3):229–233, 2013.

[19] J-S Lee, S-J Yoon, H Rah, M Tame, C Rockstuhl, S. H Song, C Lee, and K-G Lee. Quantum plasmonic sensing using single photons. *Opt. Express*, 26(22):29272, 2018.

[20] K. T Mpofu, C Lee, G. E. M Maguire, H. G Kruger, and M. S Tame. Measuring kinetic parameters using quantum plasmonic sensing. *Phys. Rev. A*, 105(3):032619, 2022.

[21] S. E Venegas-Andraca and J. L Ball. Processing images in entangled quantum systems. *Quantum Inf. Process.*, 9(1):1–11, 2010.

[22] C Moodley and A Forbes. Advances in quantum imaging with machine intelligence. *Laser Photon. Rev.*, 18(8):2300939, 2024.

[23] J Yin, Y-H Li, S-K Liao, M Yang, Y Cao, L Zhang, J-G Ren, W-Q Cai, W-Y Liu, S-L Li, and R Shu. Entanglement-based secure quantum cryptography over 1,120 kilometres. *Nature*, 582(7813):501–505, 2020.

[24] C Schimpf, M Reindl, D Huber, B Lehner, S. F Covre Da Silva, S Manna, M Vyvlecka, P Walther, and A Rastelli. Quantum cryptography with highly entangled photons from semiconductor quantum dots. *Sci. Adv.*, 7(16):eabe8905, 2021.

[25] A Forbes, M Youssef, S Singh, I Nape, and B Ung. Quantum cryptography with structured photons. *Appl. Phys. Lett.*, 124(11), 2024.

[26] N Brunner, M Huber, N Linden, S Popescu, R Silva, and P Skrzypczyk. Entanglement enhances cooling in microscopic quantum refrigerators. *Phys. Rev. E*, 89(3):032115, 2014.

[27] F Tacchino, A Auffèves, M. F Santos, and D Gerace. Steady state entanglement beyond thermal limits. *Phys. Rev. Lett.*, 120(6):063604, 2018.

[28] R Jozsa and N Linden. On the role of entanglement in quantum-computational speed-up. *Proc. R. Soc. Lond.*, 459(2036):2011–2032, 2003.

[29] Q Zhao, Y Zhou, and A. M Childs. Entanglement accelerates quantum simulation. *Nat. Phys.*, pages 1–8, 2025.

[30] D Bouwmeester, J-W Pan, K Mattle, M Eibl, H Weinfurter, and A Zeilinger. Experimental quantum teleportation. *Nature*, 390(6660):575–579, 1997.

[31] X-H Jiang, P Chen, K-Y Qian, Z-Z Chen, S-Q Xu, S-N Xie, Y-Band Zhu, and X-S Ma. Quantum teleportation mediated by surface plasmon polariton. *Sci. Rep.*, 10(1):11503, 2020.

[32] Z Deng, O Schulz, S Lin, B Ding, X Liu, X Wei, R Ros, H Yan, and Y Liu. Aqueous synthesis of zinc blende CdTe/CdS magic-core/thick-shell tetrahedral-shaped nanocrystals with emission tunable to near-infrared. *J. Am. Chem. Soc.*, 132(16):5592–5593, 2010.

[33] M Friesen, P Rugheimer, D. E Savage, M. G Lagally, D. W van der Weide, R Joynt, and M. A Eriksson. Practical design and simulation of silicon-based quantum-dot qubits. *Phys. Rev. B*, 67(12):121301, 2003.

[34] M. A Eriksson, S. N Coppersmith, and M. G Lagally. Semiconductor quantum dot qubits. *MRS bulletin*, 38(10):794–801, 2013.

[35] Z Zhou, Y Li, Z Wu, X Ma, S Fan, and S Huang. The exchange interaction between neighboring quantum dots: physics and applications in quantum information processing. *J. Semicond.*, 45(10):101701, 2024.

[36] R. D Artuso and G. W Bryant. Quantum dot–quantum dot interactions mediated by a metal nanoparticle: Towards a fully quantum model. *Phys. Rev. B*, 87(12):125423, 2013.

[37] J. D Cox, M. R Singh, G Gumbs, M. A Anton, and F Carreno. Dipole-dipole interaction between a quantum dot and a graphene nanodisk. *Phys. Rev. B*, 86(12):125452, 2012.

[38] E Waks and D Sridharan. Cavity QED treatment of interactions between a metal nanoparticle and a dipole emitter. *Phys. Rev. A*, 82(4):043845, 2010.

[39] D Zhao, Y Gu, H Chen, J Ren, T Zhang, and Q Gong. Quantum statistics control with a plasmonic nanocavity: Multimode-enhanced interferences. *Phys. Rev. A*, 92(3):033836, 2015.

[40] L. C Ugwuoke, T. P. J Krüger, and M. S Tame. Quantum plasmonics model of refractive index sensing using photon correlations. *Phys. Rev. A*, 110(4):043506, 2024.

[41] Y. V Vladimirova and V. N Zadkov. Quantum optics in nanostructures. *Nanomaterials*, 11(8):1919, 2021.

[42] A Caillas, S Suffit, P Filloux, E Lhuillier, and A Degiron.

Anomalous absorption in arrays of metallic nanoparticles: A powerful tool for quantum dot optoelectronics. *Nano Lett.*, 22(5):2155–2160, 2022.

[43] Y-H Chan, J Chen, S. E Wark, S. L Skiles, D. H Son, and J. D Batteas. Using patterned arrays of metal nanoparticles to probe plasmon enhanced luminescence of CdSe quantum dots. *ACS Nano*, 3(7):1735–1744, 2009.

[44] A. F Koenderink. Plasmon nanoparticle array waveguides for single photon and single plasmon sources. *Nano Lett.*, 9(12):4228–4233, 2009.

[45] M. L Brongersma, J. W Hartman, and H. A Atwater. Electromagnetic energy transfer and switching in nanoparticle chain arrays below the diffraction limit. *Phys. Rev. B*, 62(24):R16356, 2000.

[46] L Zhao, K. L Kelly, and G. C Schatz. The extinction spectra of silver nanoparticle arrays: influence of array structure on plasmon resonance wavelength and width. *J. Phys. Chem. B*, 107(30):7343–7350, 2003.

[47] S. A Maier, P. G Kik, H. A Atwater, S Meltzer, E Harel, B. E Koel, and A. A. G Requicha. Local detection of electromagnetic energy transport below the diffraction limit in metal nanoparticle plasmon waveguides. *Nat. Mater.*, 2(4):229–232, 2003.

[48] S Zou and G. C Schatz. Metal nanoparticle array waveguides: proposed structures for subwavelength devices. *Phys. Rev. B*, 74(12):125111, 2006.

[49] S. Y Park and D Stroud. Surface-plasmon dispersion relations in chains of metallic nanoparticles: An exact quasistatic calculation. *Phys. Rev. B*, 69(12):125418, 2004.

[50] S. A Maier. *Plasmonics: Fundamentals and Applications*. Springer, New York, 2007.

[51] C Lee, M Tame, J Lim, and J Lee. Quantum plasmonics with a metal nanoparticle array. *Phys. Rev. A*, 85(6):063823, 2012.

[52] H Kitching, M. J Shiers, A. J Kenyon, and I. P Parkin. Self-assembly of metallic nanoparticles into one dimensional arrays. *J. Mater. Chem. A*, 1(24):6985–6999, 2013.

[53] M Février, P Gogol, J-M Lourtioz, and B Dagens. Metallic nanoparticle chains on dielectric waveguides: coupled and uncoupled situations compared. *Opt. Express*, 21(21):24504–24513, 2013.

[54] V. G Bordo. Quantum plasmonics of metal nanoparticles. *J. Opt. Soc. Am. B*, 36(2):323–332, 2019.

[55] L Chen, B Su, and L Jiang. Recent advances in one-dimensional assembly of nanoparticles. *Chem. Soc. Rev.*, 48(1):8–21, 2019.

[56] J Hou, K Slowik, F Lederer, and C Rockstuhl. Dissipation-driven entanglement between qubits mediated by plasmonic nanoantennas. *Phys. Rev. B*, 89(23):235413, 2014.

[57] K. V Nerkararyan and S. I Bozhevolnyi. Entanglement of two qubits mediated by a localized surface plasmon. *Phys. Rev. B*, 92(4):045410, 2015.

[58] M Otten, R. A Shah, N. F Scherer, M Min, M Pelton, and S. K Gray. Entanglement of two, three, or four plasmonically coupled quantum dots. *Phys. Rev. B*, 92(12):125432, 2015.

[59] E Dumitrescu and B Lawrie. Antibunching dynamics of plasmonically mediated entanglement generation. *Phys. Rev. A*, 96(5):053826, 2017.

[60] M Otten, S. K Gray, and G. V Kolmakov. Optical detection and storage of entanglement in plasmonically coupled quantum-dot qubits. *Phys. Rev. A*, 99(3):032339, 2019.

[61] D Martin-Cano, A González-Tudela, L Martín-Moreno, F. J García-Vidal, C Tejedor, and E Moreno. Dissipation-driven generation of two-qubit entanglement mediated by plasmonic waveguides. *Phys. Rev. B*, 84(23):235306, 2011.

[62] Y Li, A Nemilentsau, and C Argyropoulos. Resonance energy transfer and quantum entanglement mediated by epsilon-near-zero and other plasmonic waveguide systems. *Nanoscale*, 11(31):14635–14647, 2019.

[63] H Qiu, Y You, X-H Guan, X-J Du, J He, and Z-J Yang. Efficient entanglement between two long-distance quantum emitters mediated by dark-gap-plasmon waveguides. *Phys. Rev. B*, 110(7):075432, 2024.

[64] E Altewischer, M. P Van Exter, and J. P Woerdman. Plasmon-assisted transmission of entangled photons. *Nature*, 418(6895):304–306, 2002.

[65] E Moreno, F. J García-Vidal, D Daniel Erni, and L Cirac, J. I and Martín-Moreno. Theory of plasmon-assisted transmission of entangled photons. *Phys. Rev. Lett.*, 92(23):236801, 2004.

[66] A Vivas-Viaña, D Martín-Cano, and C. S Muñoz. Dissipative stabilization of maximal entanglement between nonidentical emitters via two-photon excitation. *Phys. Rev. Res.*, 6(4):043051, 2024.

[67] W. K Wootters. Entanglement of formation and concurrence. *Quantum Inf. Comput.*, 1(1):27–44, 2001.

[68] H. J Carmichael. *Statistical methods in quantum optics I: master equations and Fokker-Planck equations*. Springer Science & Business Media, 2013.

[69] S Kadkhodazadeh, T Christensen, M Beleggia, N. A Mortensen, and J. B Wagner. The substrate effect in electron energy-loss spectroscopy of localized surface plasmons in gold and silver nanoparticles. *ACS Photonics*, 4(2):251–261, 2017.

[70] J. R Johansson, P. D Nation, and F Nori. Qutip: An open-source python framework for the dynamics of open quantum systems. *Comput. Phys. Commun.*, 183(8):1760–1772, 2012.

[71] C. H Bennett, G Brassard, S Popescu, B Schumacher, J. A Smolin, and W. K Wootters. Purification of noisy entanglement and faithful teleportation via noisy channels. *Phys. Rev. Lett.*, 76(5):722, 1996.

[72] Z Zhao, T Yang, Y-A Chen, A-N Zhang, and J-W Pan. Experimental realization of entanglement concentration and a quantum repeater. *Phys. Rev. Lett.*, 90(20):207901, 2003.

[73] P Hyllus, W Laskowski, R Krischek, C Schwemmer, W Wieczorek, H Weinfurter, L Pezzé, and A Smerzi. Fisher information and multiparticle entanglement. *Phys. Rev. A*, 85(2):022321, 2012.

[74] G Tóth, T Vértesi, P Horodecki, and R Horodecki. Activating hidden metrological usefulness. *Phys. Rev. Lett.*, 125(2):020402, 2020.

[75] R Trényi, Á Lukács, P Horodecki, R Horodecki, T Vértesi, and G Tóth. Activation of metrologically useful genuine multipartite entanglement. *New J. Phys.*, 26(2):023034, 2024.

[76] D DeMille, N. R Hutzler, A. M Rey, and T Zelevinsky. Quantum sensing and metrology for fundamental physics with molecules. *Nat. Phys.*, 20(5):741–749, 2024.

[77] C Lee, B Lawrie, R Pooser, K-G Lee, C Rockstuhl, and M Tame. Quantum plasmonic sensors. *Chem. Rev.*, 121(8):4743–4804, 2021.